

## Article

# Finite Element Analysis and Experimental Verification of Thermal Fatigue of W-PFM with Stacked Structure

Chao Qi <sup>1</sup>, Yanfei Qi <sup>2</sup> , Hanfeng Song <sup>1</sup>, Xiao Wang <sup>1</sup>, Shanqu Xiao <sup>1</sup> and Bo Wang <sup>1,\*</sup><sup>1</sup> Faculty of Materials and Manufacturing, Beijing University of Technology, Beijing 100124, China<sup>2</sup> College of Metallurgy and Energy, North China University of Science and Technology, Tangshan 063210, China

\* Correspondence: wangbo@bjut.edu.cn

**Abstract:** As the prime candidate for plasma-facing materials (PFM), the response of tungsten (W) to thermal shock loads is an important research topic for future fusion devices. Under heat loads, the surface of tungsten plasma-facing materials (W-PFM) can experience thermal damage, including brittle cracking and fatigue cracks. Therefore, exploring solutions for thermal damage of W-PFM remains one of the current research focuses. We propose a novel approach to mitigate thermal radiation damage in PFM, namely, the stacked structure W-PFM. The surface thermal stress distribution of the stacked structure W-PFM under heat loads was simulated and analyzed by the finite element method. As the foil thickness decreases, both the peak thermal stresses in the normal direction (ND) and rolling direction (RD) decrease. When the thickness decreases to a certain value, the peak thermal stress in the RD decreases to about 1384 MPa and no longer decreases; while the peak thermal stress in the ND approaches 0 MPa and can be neglected. In the range of approximately 5–100 mm, the accumulated equivalent plastic strain decreases sharply as the thickness decreases; in other thickness ranges, it decreases slowly. Thermal fatigue experiments were conducted on the stacked structure W composed of W foils with different thicknesses and bulk W using an electron beam facility. The samples were applied with a power density of 30 MW/m<sup>2</sup> for 10,000 and 20,000 pulses. The cracks on the surface of the stacked structure W extended along the ND direction, while on the surface of bulk W, besides the main crack in the ND direction, a crack network also formed. The experimental results were consistent with finite element simulations. When the pulse number was 10,000, as the thickness of the W foil decreased, the number and width of the cracks on the surface of the stacked structure W decreased. Only four small cracks were present on the surface of stacked structure W (0.05 mm). When the pulse number increased to 20,000, the plastic deformation and number of cracks on the surface of all samples increased. However, the stacked structure W (0.05 mm) only added one small crack and had the smallest surface roughness (Ra = 1.536 μm). Quantitative analysis of the fatigue cracks showed that the stacked structure W-PFM (0.05 mm) exhibited superior thermal fatigue performance.



**Citation:** Qi, C.; Qi, Y.; Song, H.; Wang, X.; Xiao, S.; Wang, B. Finite Element Analysis and Experimental Verification of Thermal Fatigue of W-PFM with Stacked Structure. *Metals* **2024**, *14*, 555. <https://doi.org/10.3390/met14050555>

Academic Editor: Hannu Hänninen

Received: 26 March 2024

Revised: 29 April 2024

Accepted: 6 May 2024

Published: 8 May 2024

**Keywords:** plasma facing materials; tungsten; thermal fatigue; irradiation effect; fusion

**Copyright:** © 2024 by the authors. Licensee MDPI, Basel, Switzerland. This article is an open access article distributed under the terms and conditions of the Creative Commons Attribution (CC BY) license (<https://creativecommons.org/licenses/by/4.0/>).

## 1. Introduction

As the prime candidate for PFM, the response of W to thermal shock loads is an important research topic for future fusion devices [1,2]. According to current tokamak designs, during normal operation, especially in the divertor region, W-PFMs must withstand harsh fusion environments, including high fluxes of low-energy particles (H/He) and neutron irradiation, as well as extreme heat loads and repeated severe thermal shocks generated by long-pulse discharges [3–5]. Under cyclic thermal loading, the surface of W-PFMs will experience thermal damage, such as brittle cracking and fatigue cracks [6,7]. These crack damages may worsen during the service life of W-PFMs, eventually leading to their degradation and failure, and even affecting the stability of the plasma.

Limiting crack propagation or increasing the ductility of W can address this issue. Previous studies include: alloying W with other elements (such as Ta, Re) [8–10], cold-rolling W [11,12], fine-grain reinforced W [11,13], using fiber-reinforced composites ( $W_f/W$ ) [14,15], or laminated W composites [16]. However, a common drawback of all these approaches is their stability issue over time and use. The most apparent problem is the transmutation of W (e.g., into Re, Os) due to neutron irradiation, which can seriously affect the possibility of maintaining the achieved ductility during fusion reactor operation. In addition, the voids and bubbles created with plasma irradiation can also affect the ductility of the material. Considering the unavoidable recrystallization (especially in experimental tokamaks like ITER), PFM solutions that rely on specific grain structures (such as texture strengthening, fine-grain strengthening) to achieve certain ductility will also face the same challenge. However, there is currently no effective method to comprehensively improve the thermal radiation damage of W-PFMs and extend its service life. Therefore, exploring solutions for thermal radiation damage of W-PFMs remains one of the current research focuses.

Terra et al. [17,18] proposed micrometer-structured W, which can significantly reduce the periodic thermal stresses near the W surface, thereby reducing surface cracking of W-PFMs. Based on a similar concept, we previously proposed a new approach to mitigate thermal fatigue damage of W-PFMs by stacking many W foils parallel to the direction of thermal loading to form a stacked structure W, replacing bulk W material. This allows the bulk W to be composed of multiple mesoscale W foils to improve the micro-load environment during service, thereby reducing the peak thermal stress and alleviating thermal fatigue damage [19,20]. We have verified the feasibility of the stacked structure PFMs on Cu materials [21] and confirmed that this structure can suppress the surface blistering effect of W at the grain scale [22].

In this work, the finite element method is used to simulate and analyze the surface thermal stress and strain distribution of the stacked structure W and bulk W with different thicknesses. Then, thermal fatigue experiments using an electron beam are conducted to study the surface thermal damage and crack distribution characteristics of the stacked structure W with different foil thicknesses under thermal loading to verify the simulation results. Subsequently, the crack evolution of the stacked structure W and bulk W under different thermal cycling numbers is studied.

## 2. Experimental and Finite Element Simulation Methods

### 2.1. Sample Preparation

The W materials used in the experiments included bulk W and W foils, both provided by Antai Technology Co., Ltd. (Xiamen, China). Both were rolled W (purity > 99.9 wt%) with dimensions of 10 mm × 10 mm. The thicknesses of the W foils were 0.05 mm and 0.1 mm, respectively, while the bulk W sample was a 3 mm thick W plate. We define the normal direction (ND) as the thickness direction of the foil, the rolling direction (RD) as the length direction of the foil, and the transverse direction (TD) as the height direction of the foil. The scheme of the laminated structure W-PFM is shown in Figure 1a. A large number of tungsten foils are stacked vertically on the copper alloy surface and compressed together using a stainless steel clamp. They are connected to the copper alloy by brazing to form a stacked structure W-PFM, with the irradiated surface (plasma-facing surface) composed of the edges of multiple foils. Since the actual foils all have a certain degree of unevenness, the average gap between the foils can be adjusted by controlling the pressure applied by the stainless steel clamp. In this work, we study the stress condition of the plasma-facing surface under transient thermal loading, and the heat transfer distance along the TD direction is smaller than the size of the tungsten foil in the TD direction, so the influence of the copper alloy can be ignored. Therefore, we only stacked them together using a stainless steel clamp without brazing them to the copper alloy. At the same time, for easy comparison with bulk W, we combined the W foils with bulk W and applied uniform pressure using a stainless steel clamp to prepare a composite experimental sample of stacked structure W and bulk W, as shown in Figure 1b. The red area in Figure 1b

represents the heat load region, i.e., the plasma-facing surface. The heat load region of the samples was mechanically polished and electrochemically polished (2 wt% NaOH solution) to a low roughness of  $R_a \approx 0.01 \mu\text{m}$ . The physical diagram of the experimental sample is shown in Figure 1c, with the red region being the thermally loaded region.

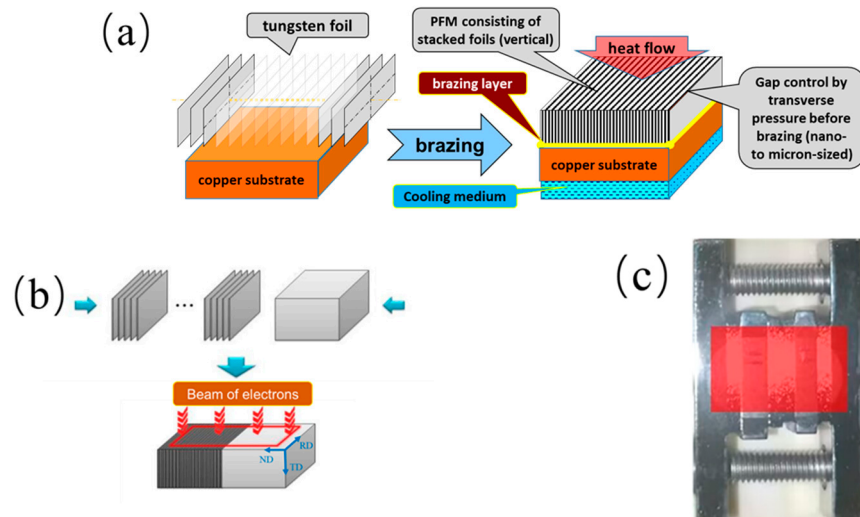


**Figure 1.** (a) Schematic of laminated structure W-PFM, (b) Schematic diagram of stacked structure W sample assembly, (c) Experimental samples of the physical picture.

## 2.2. Finite Element Simulation Analysis

### 2.2.1. Model

The stacked structure W-PFM was composed of numerous W foils, and each W foil has the same experimental environment, we select a single W foil for simulation [17]. We mainly study the effect of thickness (dimension in the ND direction) variation on surface thermal stress, and since the dimension in the RD direction is the same, we ignore its effect on surface thermal stress and choose a plane strain model. At the same time, this is also to simplify the calculation. The model size in the TD direction is set to 10 mm, which is larger than the heat transfer distance of the transient heat flow, to avoid the influence of the constant temperature boundary condition at the bottom on the temperature of the heat-loaded surface [23]. The dimensions in the ND direction are respectively 0.05, 0.1, 0.5, 1, 5, 10, 20, 50, 100, 200, and 500 mm. According to spatial symmetry, we select a 1/2 model for analysis. The mesh size of all models is uniformly  $2.5 \times 10^{-5} \text{ m}$ . Since the dimension values in the ND direction span several orders of magnitude (0.05–500 mm), the mesh size is very small, so the model images after mesh division cannot be displayed one by one here. Figure 2 shows the plane strain model image with a thickness of 5 mm.

### 2.2.2. Boundary Conditions and Thermal Property Parameters

A transient analysis of 20.5 s (heating 0.5 s/cooling 20 s) is performed on the model to simulate a complete thermal cycle. The initial temperature of the model is set to  $20 \text{ }^\circ\text{C}$ , and a heat flux density of  $30 \text{ MW/m}^2$  is loaded on the top surface (as shown by the red arrow in Figure 2). The thermal radiation effect from tungsten to the surrounding environment is ignored, so the TD surface and ND surface of the single-foil model are set to be adiabatic; at this time, the model is one-dimensional heat transfer, which can better reflect the effect of the thickness variation of the stacked structure W-PFM on the surface thermal stress. The bottom surface is assumed to be an ideal cooling condition (constant temperature of  $20 \text{ }^\circ\text{C}$ ) [23]. The mechanical constraint is a fixed constraint applied to the bottom surface of the model.

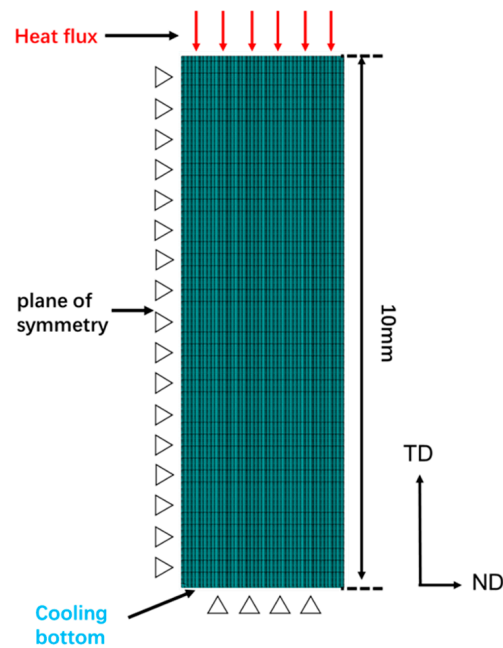


Figure 2. Schematic diagram of finite element analysis model.

Assuming *W* is an ideal elastic-plastic material, its thermal property parameters are listed in Table 1, referring to the ITER materials handbook [24] and relevant literature [25].

Table 1. Relevant parameters of tungsten finite element simulation.

Material	Temperature (°C)	Thermal Conductivity (W/(m·K))	Coefficient of Thermal Expansion ( $10^{-6}/^{\circ}\text{C}$ )	Young's Modulus (GPa)	Poisson's Ratio	Yield Strength (MPa)
W	20	173	4.50	398	0.279	1384
	500	133	4.68	390	0.284	854
	1000	111	4.89	368	0.29	465
	1500	101	5.13	306	0.295	204

### 2.3. Thermal Fatigue Experiment

The thermal fatigue tests were conducted on an electron beam facility with a rated voltage of 8 kV (a vacuum of  $4 \times 10^{-4}$  Pa). All samples were mounted in graphite crucibles placed on water-cooled copper blocks. To ensure good thermal conduction, a small amount of gallium metal was filled between the samples and the crucibles [26]. The TD surface served as the irradiated surface, and thermal cycling tests were performed for 10,000 and 20,000 cycles with a power density of  $30 \text{ MW/m}^2$ , a pulse width of 0.5 s, and a pulse interval of 20 s. The schematic diagram of the thermal fatigue device is shown in Figure 3.

The heat flux factor  $F_{\text{HF}}$  is applicable for comparing thermal shock experiments performed at different pulse durations on different devices [7]. In ITER, the time scale of transient thermal load is around 1 ms. According to the heat flux factor formula:

$$F_{\text{HF}} = P\sqrt{\Delta t} \quad (1)$$

where  $P$  is the power density and  $\Delta t$  is the heat loading duration. Our thermal fatigue experiment is equivalent to an experiment with a power density of  $670 \text{ MW/m}^2$  and a pulse duration of 1 ms.

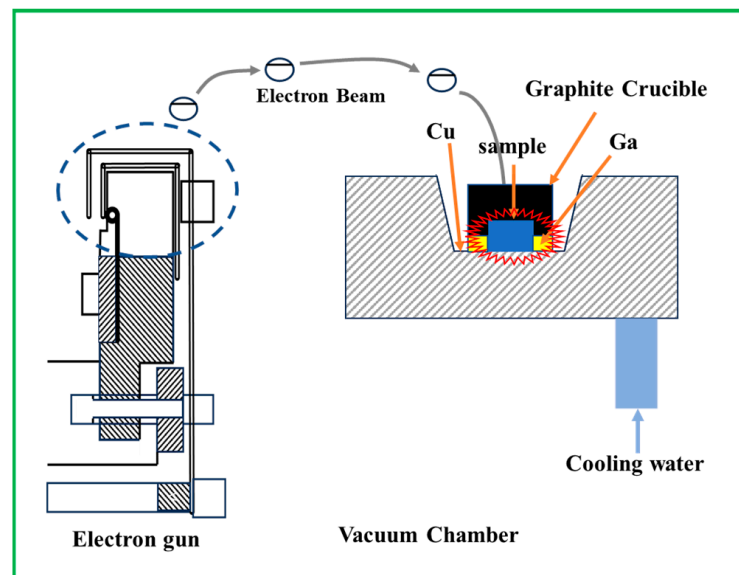


**Figure 3.** Schematic diagram of thermal fatigue testing device.

We theoretically estimated the maximum surface temperature using the following formula:

$$T_{\max} = T_0 + 2P\sqrt{(t/\pi\lambda\rho C)} \quad (2)$$

where  $T_{\max}$  is the maximum surface temperature due to the transient thermal load,  $T_0$  is the initial surface temperature,  $P$  is the power density ( $\text{W}/\text{m}^2$ ),  $t$  is the pulse duration (s),  $\lambda$  is the thermal conductivity ( $\text{W}/(\text{m}\cdot\text{K})$ ),  $\rho$  is the density ( $\text{kg}/\text{m}^3$ ), and  $C$  is the specific heat ( $\text{J}/(\text{kg}\cdot\text{K})$ ). This has been proven to be an effective method for theoretically calculating the maximum surface temperature under thermal loading [7,27,28]. Using the thermal properties at 20 °C and 1500 °C, the estimated surface temperature range was 1173–1351 °C.

#### 2.4. Characterization Methods and Performance Measurements

The surface morphology of the samples before and after thermal fatigue tests was examined by Scanning Electron Microscope (SEM, FEI Quanta650FEG, Hillsboro, OR, USA). The metallographic structure of the samples before thermal fatigue tests was obtained by optical microscope (OLYMPUS DP27, Tokyo, Japan). The surface roughness ( $R_a$ ) of the samples after thermal fatigue tests was obtained by laser confocal microscope (OLYMPUS-LEXT-OLS4000, Tokyo, Japan), with the test details shown in Figure 4. To avoid the influence of the foil gap on the test, the sampling lines were parallel to the RD, and the sampling line of the foil was located in the ND center area. Each W foil was sampled once, and 5 foils were sampled to report the average value. The bulk W was also sampled 5 times to report the average value.

After the thermal fatigue test, Vickers microhardness testing was performed on the ND surface of the heat-loaded center area of the bulk W. The sample was subjected to Vickers microhardness testing (MH-50) at room temperature, with a load of 100 g and a dwell time of 15 s [29]. Starting from 50  $\mu\text{m}$  away from the heat-loaded surface, a group of tests (indentations parallel to the TD surface) was performed every 100  $\mu\text{m}$  along the TD direction until the hardness value tended to be stable. All indentations were optically inspected, and unsuitable indentations were eliminated. For each group of 5 hardness values, the average hardness value was reported.

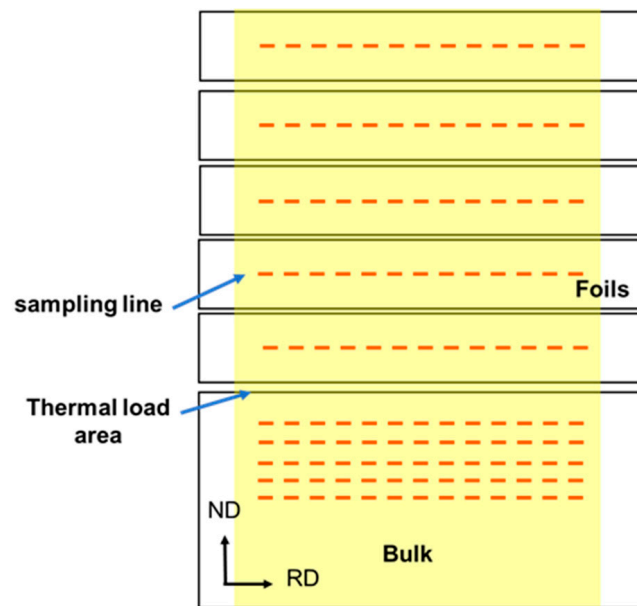


**Figure 4.** Schematic diagram of roughness test. The yellow area is the thermal load area and the red dotted lines are the sampling line.

### 3. Finite Element Simulation of Stacked Structure W-PFM

Since the heat transfer is a one-dimensional model, the highest temperature is the surface temperature. We neglected the thermal radiation effect and the thickness of the model has no effect on its temperature distribution, so the temperature distribution is the same in the TD direction for models with different thicknesses. Figure 5 shows the evolution of the temperature distribution of the loaded surface over time for a single cycle of the bulk model at  $30 \text{ MW/m}^2$  heat flux, with a maximum temperature of  $1251 \text{ }^\circ\text{C}$ . The simulated surface temperature is within the range of theoretically estimated surface temperature, indicating that the temperature results of our simulation are reasonable.

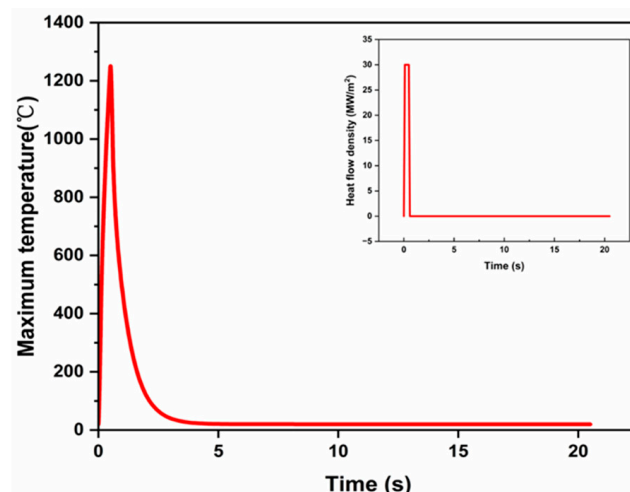


**Figure 5.** Evolution of the maximum temperature of the thermally loaded surface with time.

As shown in Figure 6, the peak thermal stresses on the heat-loaded surface in the RD and ND directions are compared for models with different thicknesses. As the thickness decreases, the peak stresses on the heat-loaded surface in the RD and ND directions both decrease in an “S” curve shape. When the thickness decreases to  $0.5 \text{ mm}$ , the decrease in peak thermal stress in the RD slows down, with the peak thermal stress in the RD decreasing by about  $214 \text{ MPa}$ , and the stress value is close to the yield strength of the

material, as shown in Figure 6a. The peak thermal stress in the ND is close to 0 MPa and can be neglected, with the peak thermal stress in the ND decreasing by about 1384 MPa, which is close to the yield strength of the material, as shown in Figure 6b. This is because when the model thickness is large, there are relatively large peak thermal stresses in both the ND and RD directions. The stress state on the heat-loaded surface is a two-dimensional stress state, as shown in Figure 7a. After multiple cycles of thermal loading, it is expected that cracks will form on the heat-loaded surface in both the ND and RD directions. As the thickness decreases to a certain value, the peak thermal stress in the ND decreases to approximately 0 MPa and can be neglected, with only a certain stress existing in the RD direction. The stress state on the heat-loaded surface changes from a two-dimensional stress state to a uniaxial stress state, as shown in Figure 7b. At this point, the thermal damage on the heat-loaded surface of the model is mainly caused by the stress in the RD direction, and the stress in the ND does not generate thermal damage. After multiple cycles of thermal loading, it is expected that cracks will appear on the heat-loaded surface due to the stress in the RD direction only.

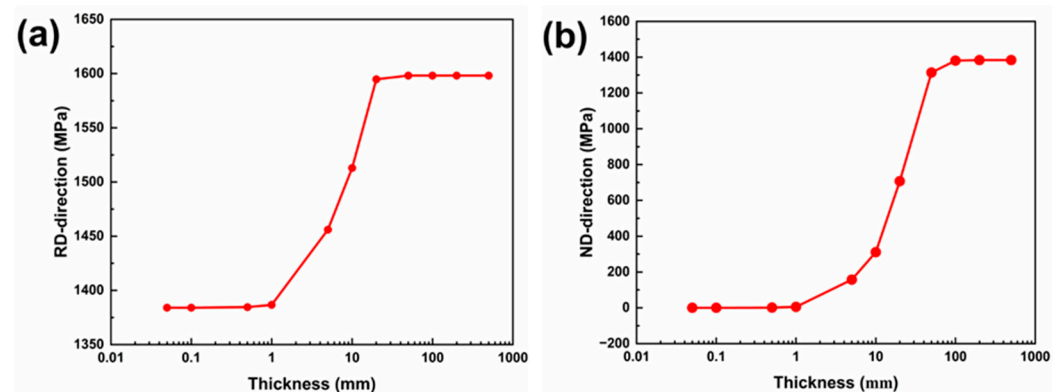


**Figure 6.** Thermally loaded surface (a) Peak thermal stress in the RD-direction as a function of thickness (b) Peak thermal stress in the ND-direction as a function of thickness.

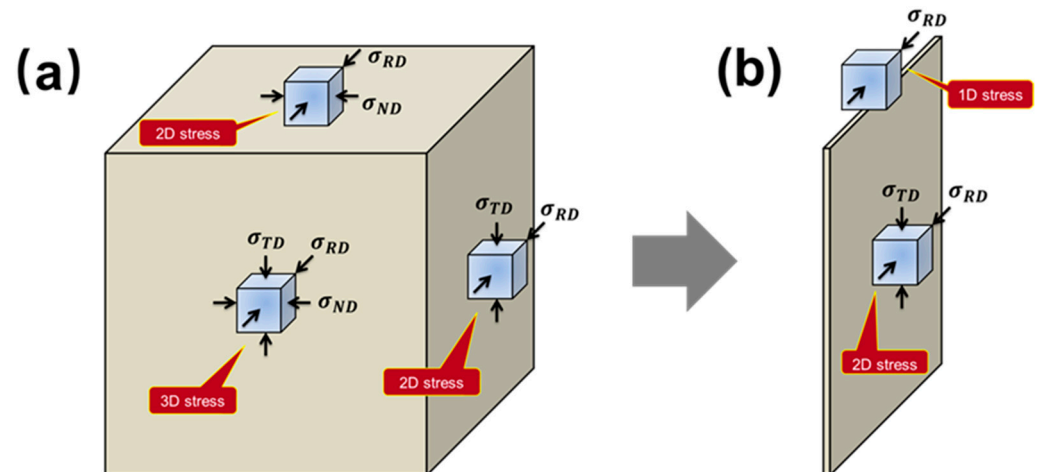


**Figure 7.** Schematic diagram of model stress state (a) Bulk stress state (b) Foil stress state.

Figure 8 shows the change in the difference in RD stress from the center to the edge along the ND direction on the heat-loaded surface of single-foil models with different thicknesses at the end of the cyclic thermal load (20.5 s). It can be seen from the figure that as the thickness decreases, the difference in RD stress along the ND direction on the heat-loaded surface decreases in an “S” curve shape. In the range of approximately 1 mm to 20 mm, the difference in RD stress on the heat-loaded surface decreases sharply as the thickness decreases. Beyond the thickness range of 20 mm, the difference in RD stress no longer changes. When the model thickness decreases to 0.1 mm, the difference in RD

stress is 0, indicating that the RD thermal stress is equal from the center to the edge. After multiple cycles of thermal loading, it is expected that the width of the cracks caused by the RD stress on the heat-loaded surface of the single-foil model with a thickness not exceeding 0.1 mm will be equal.

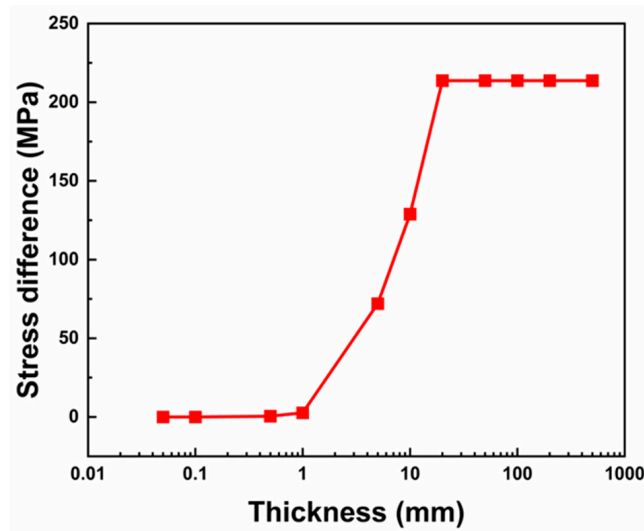


**Figure 8.** RD stress difference versus thickness curves in the ND direction on thermally loaded surfaces for bulk models.

Figure 9 shows the maximum accumulated equivalent plastic strain on the heat-loaded surface of single-foil models with different thicknesses at the end of cooling. In the range of approximately 5 mm to 100 mm, the equivalent plastic strain decreases sharply as the thickness decreases; in other thickness ranges, the equivalent plastic strain decreases slowly as the thickness decreases. The decrease in model thickness effectively reduces the equivalent plastic strain, improving the thermal fatigue resistance of the heat-loaded surface.

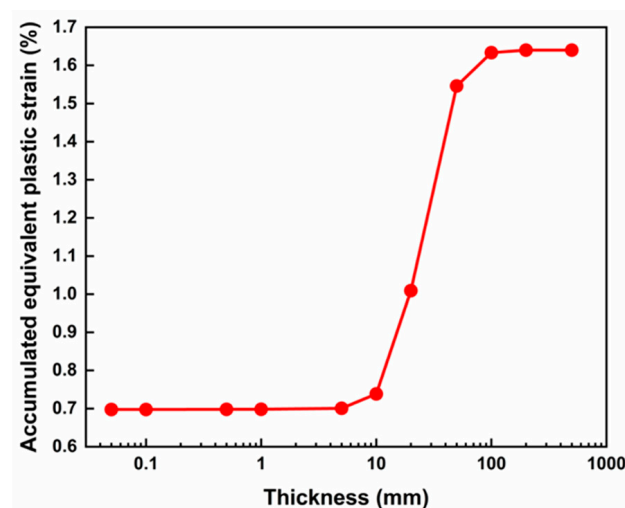


**Figure 9.** Thermally loaded surface equivalent plastic strain vs. thickness.

Through finite element simulations of the stacked structure W-PFMs, we found that reducing the foil thickness can effectively reduce the peak thermal stress on the heat load surface and the surface equivalent plastic strain, which is beneficial for improving the thermal fatigue resistance of W-PFMs.

#### 4. Thermal Fatigue Test

##### 4.1. Surface Damage Morphology Characteristics of Stacked Structure W-PFMs and Bulk W-PFMs

When the electron beam applies a thermal load to the sample, the material surface undergoes thermal expansion, which is constrained by the surrounding cooler material, generating compressive stress. If these stresses exceed the yield strength of the material, plastic deformation will occur. After heat loading, the material enters the cooling stage and undergoes contraction. Since the plastic strain gradually decreases to zero with increasing depth, the material cannot recover to its original state through elastic strain, and the compressive stress is converted into tensile stress. Due to the plastic strain generated in the material, fatigue cracks are produced. Figure 10a,b show the metallographic images of the sample surface before heat loading, with no cracks present on the surface. After 10,000 cycles of thermal loading at a power density of  $30 \text{ MW/m}^2$ , the damage morphology of the stacked structure W-PFM and bulk W-PFM surfaces is shown in Figure 10. Both stacked W and bulk W surfaces exhibit cracks along the ND direction, as indicated by the red boxes in Figure 10. The cracks on the surface of stacked W are dispersed and discontinuous, with crack propagation being interrupted, and only a single crack along the ND is observed. In contrast, the surface of bulk W exhibits cracks along both the ND and RD directions. ND cracks are wider and longer, representing the main crack. This is because the bulk W used is a 3 mm thick plate, resulting in slight differences in the ND and RD stresses, with maximum stress along the RD. Consequently, the primary crack on the surface of bulk W occurs along the ND and additional cracks along the RD, ultimately forming a crack network. As the thickness decreases, the stress on the stacked structure W in the ND decreases sharply and can eventually be neglected, with the maximum stress along the RD, and the stress state of the heat flow loading surface changes from a two-dimensional stress state to a uniaxial stress state. The surface expansion and contraction are only constrained by the RD, and the gaps between the W foils in the ND provide a stress release space, finally producing only ND fatigue cracks, as shown on the surfaces of the 0.05 mm and 0.1 mm tungsten foils in Figure 10. This is in good agreement with the stress analysis results from the finite element simulation. Comparing the cracks in the stacked structure W in Figure 10a,b, it can be seen that as the thickness decreases, the crack damage on the heat-loaded surface is alleviated, and reducing the thickness is an effective way to improve the thermal fatigue resistance of the stacked structure W.

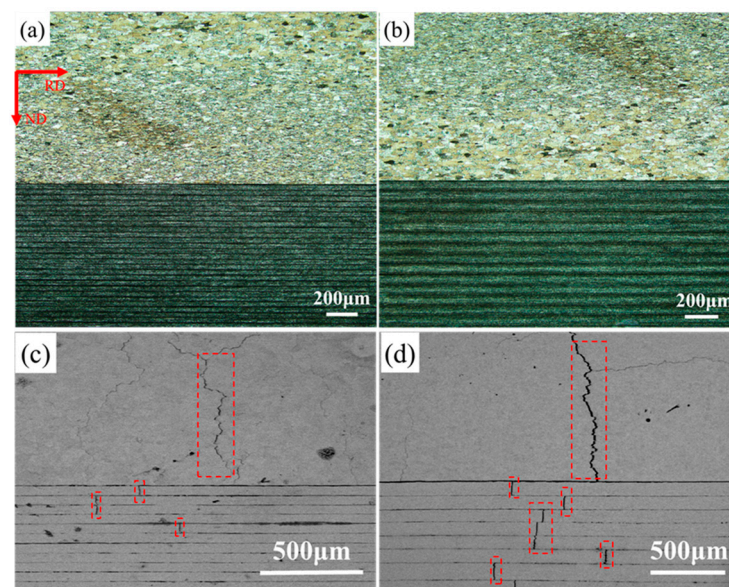


**Figure 10.** Metallographic images before thermal loading (a) stacked structure W (0.05 mm), (b) stacked structure W (0.1 mm), SEM images after thermal loading (c) stacked structure W (0.05 mm), (d) stacked structure W (0.1 mm).

#### 4.2. Comparison of Thermal Fatigue Cracking Evolution Process of the Stacked Structure W-PFM and the Bulk W-PFM

Under the condition of a power density of  $30 \text{ MW/m}^2$ , 10,000 cycles of thermal loading were first applied to the stacked structure W and bulk W, and the surface thermal damage morphology was observed and recorded. Then, another 10,000 cycles of thermal loading were performed, and the surface damage morphology was observed and recorded. We compared the surface damage morphology under the two thermal loads to study the evolution process of thermal fatigue cracks on the surfaces of the stacked structure W and bulk W. The surface thermal damage morphology is shown in Figure 11.

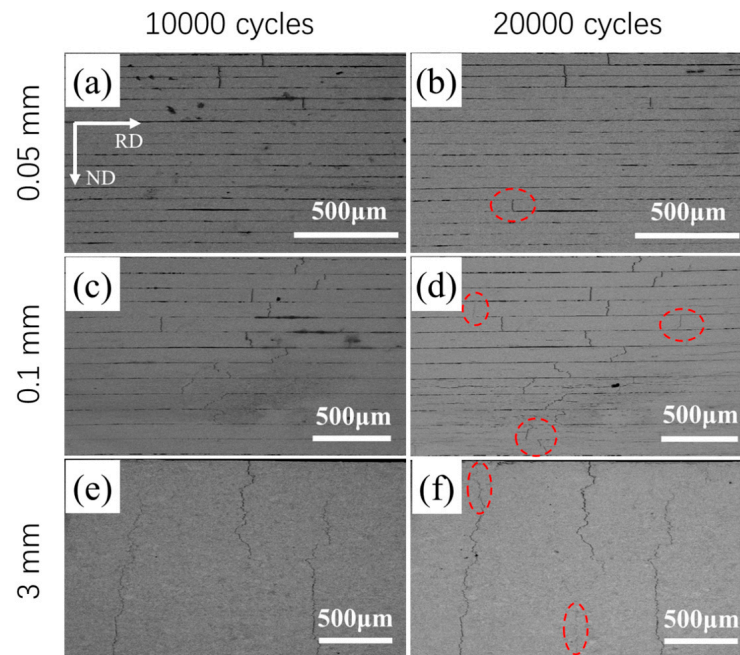


**Figure 11.** Surface damage diagrams of stacked W and bulk W-PFM under thermal load of different cycles. (a) stacked structure W (0.05 mm, 10,000 cycles), (b) stacked structure W (0.05 mm, 20,000 cycles), (c) stacked structure W (0.1 mm, 10,000 cycles), (d) stacked structure W (0.1 mm, 20,000 cycles), (e) bulk W (10,000 cycles), (f) bulk W (20,000 cycles).

As can be seen from Figure 11, under the same heat flux density, as the number of heat load cycles increases, the degree of surface damage on the stacked structure W and bulk W increases to different extents, except for the stacked structure W (0.05 mm). After 10,000 cycles of thermal loading, both stacked W and bulk W surfaces exhibit cracks. A comparison between Figure 11a,b reveals that after increasing the cycle count to 20,000 cycles, there is a slight change in the number of cracks on the surface of stacked W (0.05 mm), with an additional crack appearing, as indicated by the red marker in Figure 11b. By comparing Figure 11c,d, when the number of cycles increases to 20,000, the number of cracks on the surface of stacked W (0.1 mm) significantly increases, as shown by the red marker in Figure 11d, with new cracks appearing on the surfaces of some foils. As depicted in Figure 11e,f, there is a noticeable increasing trend in thermal fatigue damage on the surface of bulk W with an increase in the cycle count. when the number of cycles increases to 20,000, the width of the cracks on the left side of the image increases, and the cracks noticeably lengthen, as indicated by the red marker in Figure 11f. From the observed surface crack damage on W, it can be concluded that the thermal fatigue damage on stacked W remains relatively light, especially for stacked W (0.05 mm), which exhibits the least thermal damage under the cyclic thermal loading.

Compared to the low-magnification observations in Figure 11, the changes in the surface morphology of the stacked structure W and bulk W at different cycle numbers under high-magnification SEM observation are shown in Figure 12.

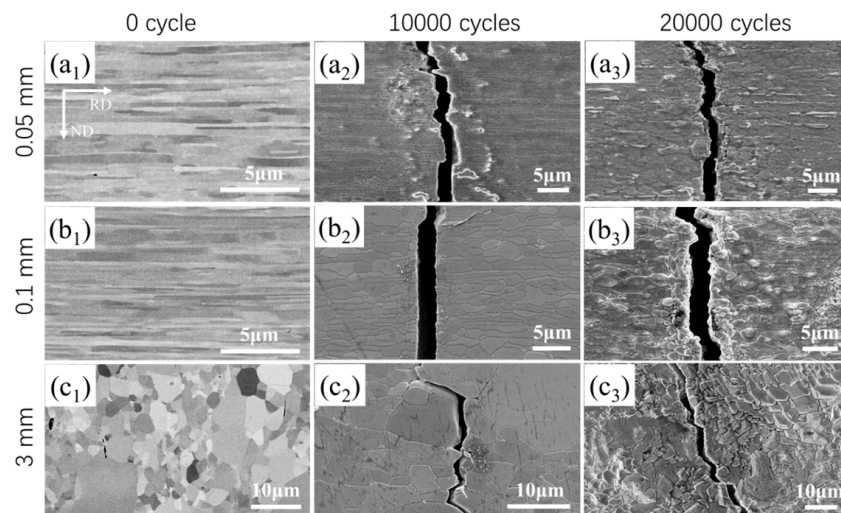


**Figure 12.** Microscopic morphology changes of W foils and bulk W surfaces with different thicknesses during thermal loading, where (a<sub>1</sub>, b<sub>1</sub>, c<sub>1</sub>) were utilized with the backscattering detector. (a<sub>2</sub>) stacked structure W (0.05 mm, 10,000 cycles), (a<sub>3</sub>) stacked structure W (0.05 mm, 20,000 cycles), (b<sub>2</sub>) stacked structure W (0.1 mm, 10,000 cycles), (b<sub>3</sub>) stacked structure W (0.1 mm, 20,000 cycles), (c<sub>2</sub>) bulk W (10,000 cycles), (c<sub>3</sub>) bulk W (20,000 cycles).

As can be seen from Figure 12, for samples with the same thickness, as the number of thermal loading cycles increases, the microscopic morphology of the stacked structure W and bulk W surfaces changes to different degrees. Under cyclic thermal loading, the fluctuating temperature causes changes in the internal stress and microstructure of the material, even leading to recovery, recrystallization, and surface roughening of the material grains. For the stacked structure W (0.05 mm), by comparing Figure 12(a<sub>1</sub>–a<sub>3</sub>), after 10,000 cycles of thermal loading, we can see that most of the grain structures on the sample surface still maintain the fibrous organization state after rolling. The surface is relatively flat, with only slight plastic deformation at the crack edges. However, after 20,000 cycles of thermal loading, some of the grain structures on the surface underwent recovery. The surface became rough, with severe plastic deformation occurring at the crack edges. Part of the grain structure exhibited an extruded state, mostly in the RD grains. This may be related to the texture introduced during the rolling process. In the experiment, the surface temperature of the loading area undergoes periodic fluctuations with cyclic thermal loading, and then cyclic alternations of compressive and tensile stresses are generated in the loading area. The shear stresses generated on the crystallographic slip planes of different grains under cyclic thermal loading are different, which is strongly related to the crystallographic orientation. When the cyclic shear stress on the slip systems of some grains on the material surface reaches a critical value, cyclic slip will occur. With the conversion of shear stress, irreversible slip will occur on the same slip band and also on adjacent parallel slip planes [26]. Therefore, in the cyclic plastic deformation process, the extruded/intruded structures/grains will extrude/intrude the surface along the crystallographic slip planes. For the stacked structure W (0.1 mm), by comparing Figure 12(b<sub>1</sub>–b<sub>3</sub>), after 10,000 cycles of thermal loading, we can find that most of the grain structures on the sample surface underwent recovery and growth, with a small portion of grains still maintaining the RD fibrous organization. The surface is relatively flat, with only slight plastic deformation at the crack edges. After 20,000 cycles of thermal loading, the recovery and grain growth phenomena on the surface became more pronounced. For the bulk W-PFM, by comparing Figure 12(c<sub>1</sub>–c<sub>3</sub>), after 10,000 cycles of thermal loading, we found that most of the grains on the sample surface still maintained the original equiaxed grain state, with no surface roughening. After 20,000 cycles of thermal loading, the surface underwent severe roughening (i.e., surface etching), exhibiting a pyramidal shape. These

pyramidal shapes are regular and have a certain angle, which should be related to the grain orientation.

For samples with the same number of thermal cycles, with increasing thickness, their microstructural morphology also changes to varying degrees. Before thermal loading, the stacked structure W (0.05 mm and 0.1 mm) exhibited elongated fibrous grains along the RD, with the grain sizes being similar and lengths ranging from a few  $\mu\text{m}$  to tens of  $\mu\text{m}$ . Along the ND, the grain boundary density was very high, as shown in Figure 12(a<sub>1</sub>,b<sub>1</sub>). In contrast, the bulk W exhibited equiaxed grains with a large variation in grain size from a few micrometers to tens of micrometers, which may be due to insufficient grain growth during the production process, as shown in Figure 12(c<sub>1</sub>). After 10,000 thermal loading cycles (Figure 12(a<sub>2</sub>–c<sub>2</sub>)), all samples exhibited cracking. The fatigue cracks on the surface of the stacked structure W (0.05 mm and 0.1 mm) propagated in a transgranular manner, with a relatively uniform crack width of approximately 2  $\mu\text{m}$ , which is consistent with our finite element simulation results of the RD stress difference (Figure 8). In contrast, the bulk W exhibited an intergranular fracture mode, with non-uniform crack widths. As pointed out by Prakash et al. [30], when the kink angle between the grain boundary and the crack propagation direction is smaller than a threshold angle (around 50°, with a higher grain boundary cohesive strength leading to a smaller threshold angle), the fracture process zone will undergo intergranular fracture; in other words, if the kink angle is larger than the threshold angle, the grains will undergo transgranular brittle fracture. As shown in Figure 13, the W foil exhibits a high density of fibrous grains along the crack propagation direction. The cracks are nearly perpendicular to the grain boundaries of the fibrous grains, resulting in a very large misorientation angle. In contrast, the bulk W consists of equiaxed grains, with most misorientation angles being relatively small. After 20,000 thermal loading cycles (Figure 12(a<sub>3</sub>–c<sub>3</sub>)), with increasing thickness, the surface roughening and plastic deformation of the samples increased, as shown in Table 2. This may be due to the larger thickness resulting in higher surface thermal stresses, and a higher degree of grain recovery and growth, leading to a more severe reduction in material strength, making this effect more pronounced. The increase in surface roughness is well reflected in the finite element simulation results of the accumulated equivalent plastic strain, indicating that reducing the thickness of the W foil can effectively reduce the surface plastic deformation under thermal loading, thereby mitigating thermal damage. The increase in surface roughness implies an increased absorption of electron beam energy at a constant power density, which in turn leads to more severe damage. It is noteworthy that the fibrous grain structure of the foil, resulting from the rolling process, may enhance the yield strength and ultimate tensile strength of the material, which is beneficial for suppressing thermal fatigue damage [31].

**Table 2.** Surface roughness of thermally loaded area (20,000).

	0.05 mm	0.1 mm	3 mm
Roughness ( $R_a/\mu\text{m}$ )	1.536	1.668	2.586

According to the estimated surface temperature of the samples, which is slightly lower than the recrystallization temperature of W (ITRR 1300 °C) [32], recrystallization was observed in the stacked W structures, as shown in Figure 12. For the bulk W, due to the large variation in grain size before thermal loading, it is difficult to determine whether recrystallization occurred from the changes in microstructure alone. As is well known, hardness is closely related to microstructure, and the evolution of hardness can reflect the recrystallization behavior of the material [33–35]. Vickers microhardness tests were performed on the ND surface of the center region of the bulk W sample subjected to thermal loading. Starting from 50  $\mu\text{m}$  away from the thermally loaded surface, a set of indentations (parallel to the surface) were made along the TD at intervals of 100  $\mu\text{m}$  until the hardness values stabilized, as shown in Figure 14. The hardness values decreased with decreasing distance from the surface. An anomaly in hardness was observed at 50  $\mu\text{m}$ , which is similar to the observation by Nemati et al. in their high heat flux tests [29]. This may be due

to the severe deformation near the surface during the experiment, resulting in a higher dislocation density and a higher fraction of low-angle grain boundaries in this region. The hardness tests indicate that recrystallization also occurred in the bulk W sample. It can be considered that the recrystallization phenomenon was accelerated by the combined effect of high thermal stresses and repeated cycling at elevated temperatures. These extreme conditions may have induced dynamic recrystallization and grain growth, thereby affecting the material's resistance to thermal fatigue. During the experimental process, the applied stress will accumulate in the form of stored energy, such as dislocations, on the material surface. The gradual increase in dislocation density may lead to stress concentrations, which can act as potential crack initiation sites, resulting in the formation of fatigue cracks on the surface. On the other hand, the stored energy may promote recrystallization, thereby lowering the recrystallization temperature to a relatively low value during repeated thermal loading [28]. However, the fibrous grain structure of the stacked W structures, along with the low stress along the RD and the crack deflection effect along the ND, contributed to their superior thermal fatigue resistance compared to the bulk W.

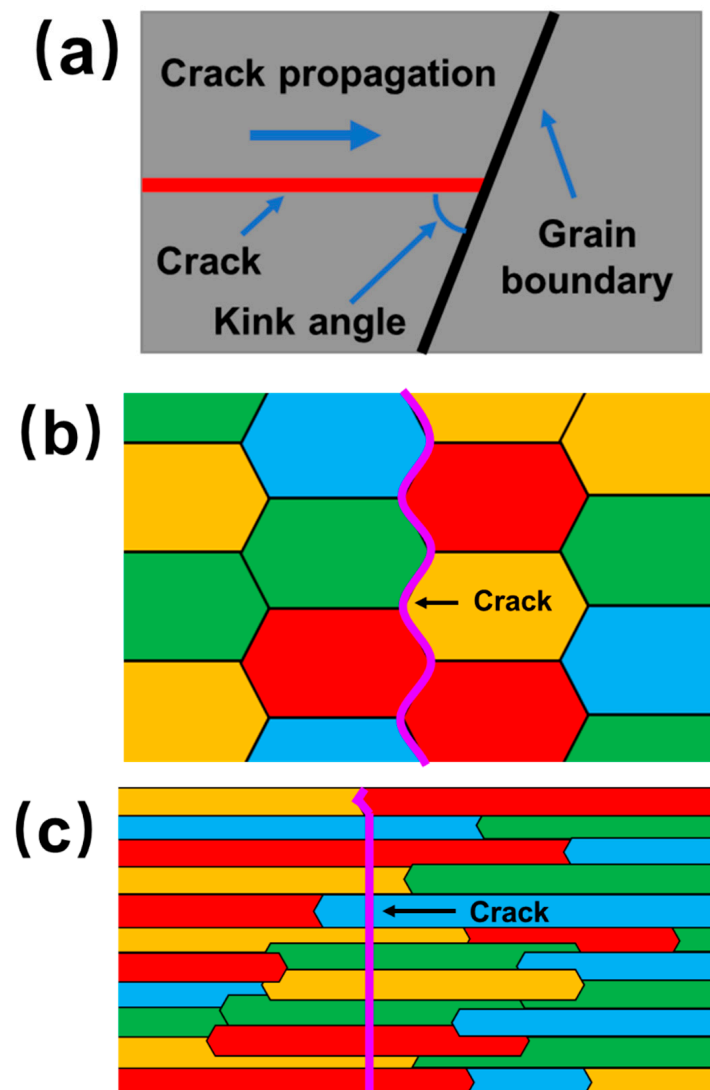


**Figure 13.** (a) Kink angle between grain boundary and crack propagation direction; (b) Bulk W and (c) W foils are the scheme of crack propagation route in TD plane.

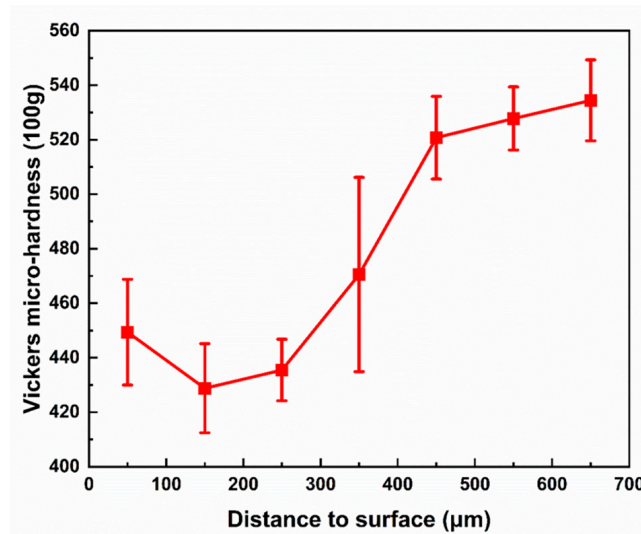


**Figure 14.** Curve of hardness with depth after thermal loading of block W (100 g).

To accurately compare the surface crack damage of samples with different thicknesses subjected to the same thermal loading after 20,000 thermal cycles, an improved quantitative analysis method (Uddholm method) was employed to evaluate the surface crack damage [36,37]. The key aspect of this method is the accurate calculation of the fatigue damage factor (D). A larger fatigue damage factor D indicates more severe surface crack damage. The fatigue damage factor is calculated using the following formula:

$$D = S \cdot W \quad (3)$$

where D is the fatigue damage factor (Twips, 17.64 μm), S is the percentage of the surface crack area (%), and W is the average width of the main surface crack (μm). SEM images at the same magnification were processed and calibrated using image software, as shown in Figure 15. The various parameters were then calculated using computational software, and the results are presented in Table 3. Under the same thermal loading conditions and after 20,000 thermal cycles, the stacked W structure (0.05 mm) exhibited the best thermal fatigue performance.

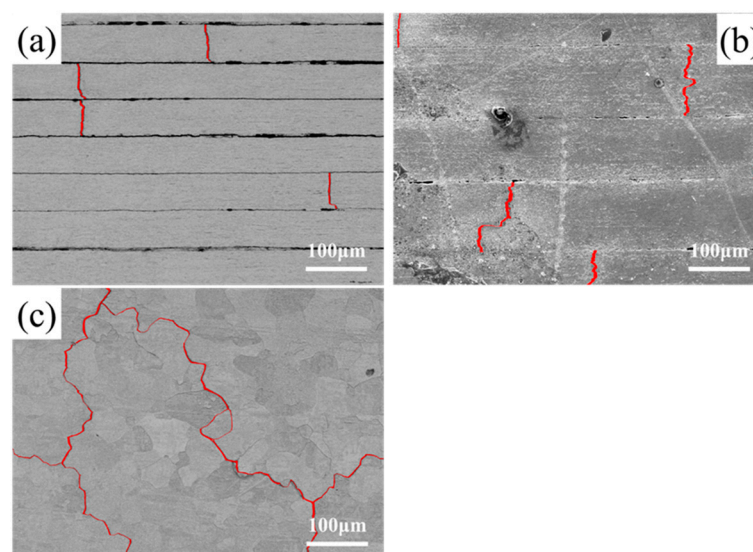


**Figure 15.** Crack calibration on the sample surface after 20,000 thermal cycles (a) 0.05 mm, (b) 0.1 mm, (c) bulk W. The red regions are surface cracks area.

**Table 3.** The calculation results of the parameters associated with the damage factor.

Samples	S/%	W/ $\mu\text{m}$	D/17.64 $\mu\text{m}$
0.05 mm	0.2089	2.4735	0.005167
0.1 mm	0.6998	3.512	0.02257
Bulk	0.8962	3.4603	0.03101

## 5. Conclusions

In this study, finite element simulations were performed to analyze the thermal stress behavior on the thermally loaded surface of stacked W-PFM structures, and the influence of thickness was investigated. When the thickness was reduced to a certain value, the peak thermal stress along the ND became negligible (close to 0 MPa), while the peak thermal stress along the RD decreased to approximately 1384 MPa and did not decrease further. In the range of approximately 5 mm to 100 mm, the equivalent plastic strain decreased rapidly with decreasing thickness, while in other thickness ranges, the equivalent plastic strain decreased slowly with decreasing thickness.

To verify the simulation results, thermal fatigue experiments were conducted on stacked W structures and bulk W samples using an electron beam facility. The surface cracks formed on the stacked W structures under cyclic thermal loading were oriented along the ND. For the bulk W, in addition to the main cracks along the ND, a crack network was also observed. These observations were consistent with the finite element simulation results. At 10,000 pulses, as the thickness of the W foil decreased, the number and width of surface cracks on the stacked W structures decreased. When the number of pulses increased to 20,000, the surface plastic deformation and the number of cracks increased for all samples. The quantitative analysis of fatigue cracks revealed that the stacked W-PFM structure (0.05 mm) exhibited superior thermal fatigue performance.

Although the current study is only a conceptual validation and not a comprehensive evaluation of a final product, the stacked structure concept offers a wide range of optimization possibilities. It can be combined with existing research methods, and the pure W foil can be replaced with other materials, such as W alloys or nanostructured W. Moreover, compared to existing research, the W foil can be manufactured using current industrial processes, without the need for expensive manufacturing techniques. Structures based on this concept may potentially solve the thermal fatigue issues faced by plasma-facing materials and extend the lifetime of PFMs. However, further research and development are required to fully realize the potential of this approach.

**Author Contributions:** Methodology, C.Q., Y.Q., H.S. and B.W.; Validation, S.X. and B.W.; Formal analysis, C.Q.; Investigation, C.Q., Y.Q. and H.S.; Resources, X.W. and B.W.; Writing—original draft, C.Q.; Writing—review & editing, X.W.; Visualization, S.X.; Supervision, B.W.; Project administration, B.W.; Funding acquisition, B.W. All authors have read and agreed to the published version of the manuscript.

**Funding:** This research was funded by the National Natural Science Foundation of China (Project No. 52104374) and by the Hebei Province Centralized Guided Local Science and Technology Development Funds Project (Project No. 236Z1004G).

**Data Availability Statement:** The raw data supporting the conclusions of this article will be made available by the authors on request.

**Acknowledgments:** The authors would like to thank Zhichao Lu for his workstation and writing assistance.

**Conflicts of Interest:** The authors declare no conflict of interest.

## References

1. Luo, C.; Xu, L.; Zong, L.; Shen, H.; Wei, S. Research Status of Tungsten-Based Plasma-Facing Materials: A Review. *Fusion Eng. Des.* **2023**, *190*, 113487. [[CrossRef](#)]

2. Nogami, S.; Hasegawa, A.; Fukuda, M.; Rieth, M.; Reiser, J.; Pintsuk, G. Mechanical Properties of Tungsten: Recent Research on Modified Tungsten Materials in Japan. *J. Nucl. Mater.* **2021**, *543*, 152506. [[CrossRef](#)]
3. Shi, J.; Song, J.; Liang, M.; Lian, Y.; Wang, J.; Feng, F.; Liu, X. Effects of Minor Rhenium Additions on the Thermal Properties and Recrystallization Temperature of Tungsten Alloy. *Nucl. Mater. Energy* **2024**, *38*, 101609. [[CrossRef](#)]
4. Yin, H.; Cheng, L.; Zhang, X.; Zhang, H.; Guo, W.; Yuan, Y.; Yan, B.; Wang, P.; Lu, G.-H. Surface Blistering and Deuterium Retention in Chemical Vapor Deposition Tungsten Exposed to Deuterium Plasma. *Nucl. Mater. Energy* **2023**, *37*, 101536. [[CrossRef](#)]
5. Xia, T.; Jiang, Z.; Shi, Y.; Ren, X.; Zhang, W.; Wang, M.; Liang, L.; Zhu, K. Surface Modification and Helium Release of Tungsten Irradiated by 40 keV Helium Ions. *Phys. Scr.* **2023**, *98*, 095604. [[CrossRef](#)]
6. Wang, Y.; Wang, H.; Mi, B.; Zhao, J.; Zhang, C. Microstructure-Based Crack Formation in Tungsten Exposed to Cyclic Transient Heating. *J. Nucl. Mater.* **2023**, *583*, 154555. [[CrossRef](#)]
7. Rieth, M.; Doerner, R.; Hasegawa, A.; Ueda, Y.; Wirtz, M. Behavior of Tungsten under Irradiation and Plasma Interaction. *J. Nucl. Mater.* **2019**, *519*, 334–368. [[CrossRef](#)]
8. Dhard, C.P.; Masuzaki, S.; Naujoks, D.; Neu, R.; Nagata, D.; Khokhlov, M. Exposure of Tungsten Heavy Alloys at High Thermal Loads in LHD. *Nucl. Mater. Energy* **2024**, *38*, 101585. [[CrossRef](#)]
9. Ren, D.; Xi, Y.; Yan, J.; Zan, X.; Luo, L.; Wu, Y. Surface Damage and Microstructure Evolution of Yttria Particle-Reinforced Tungsten Plate during Transient Laser Thermal Shock. *Metals* **2022**, *12*, 686. [[CrossRef](#)]
10. Yang, T.; Wang, J.; Feng, F.; Liu, X.; Youyun, L.; Xueyu, G. Composite Effect of Helium Ion Irradiation and Transient Thermal Shock on Recrystallized Pure W and W-Y<sub>2</sub>O<sub>3</sub> Alloys. *Fusion Eng. Des.* **2023**, *196*, 113991. [[CrossRef](#)]
11. Lied, P.; Pantleon, W.; Bonnekoh, C.; Dürrschnabel, M.; Bienert, C.; Hoffmann, A.; Reiser, J.; Rieth, M. Comparison of K-Doped and Pure Cold-Rolled Tungsten Sheets: Microstructure Restoration in Different Temperature Regimes. *Int. J. Refract. Met. Hard Mater.* **2023**, *113*, 106198. [[CrossRef](#)]
12. Reiser, J.; Hoffmann, J.; Jäntschi, U.; Klimenkov, M.; Bonk, S.; Bonnekoh, C.; Hoffmann, A.; Mrotzek, T.; Rieth, M. Ductilisation of Tungsten (W): On the Increase of Strength AND Room-Temperature Tensile Ductility through Cold-Rolling. *Int. J. Refract. Met. Hard Mater.* **2017**, *64*, 261–278. [[CrossRef](#)]
13. Liang, M.; Dai, S.; Song, J.; Yan, B.; Lian, Y.; Feng, F.; Liu, X.; Ren, P. Superior Strength-Ductility Synergy of High Potassium-Doped Tungsten Rods with Large Swaging Deformation. *Int. J. Refract. Met. Hard Mater.* **2023**, *114*, 106247. [[CrossRef](#)]
14. Neu, R.; Coenen, J.W.; Curzadd, B.; Gietl, H.; Greuner, H.; Höschen, T.; Hunger, K.; Lürbke, R.; Müller, A.; Riesch, J.; et al. Material and Component Developments for the DEMO Divertor Using Fibre Reinforcement and Additive Manufacturing. *Mater. Res. Express* **2023**, *10*, 116516. [[CrossRef](#)]
15. Coenen, J.W.; Mao, Y.; Sistla, S.; Riesch, J.; Hoeschen, T.; Broeckmann, C.; Neu, R.; Linsmeier, C. Improved Pseudo-Ductile Behavior of Powder Metallurgical Tungsten Short Fiber-Reinforced Tungsten (W/W). *Nucl. Mater. Energy* **2018**, *15*, 214–219. [[CrossRef](#)]
16. Reiser, J.; Garrison, L.; Greuner, H.; Hoffmann, J.; Weingärtner, T.; Jäntschi, U.; Klimenkov, M.; Franke, P.; Bonk, S.; Bonnekoh, C.; et al. Ductilisation of Tungsten (W): Tungsten Laminated Composites. *Int. J. Refract. Met. Hard Mater.* **2017**, *69*, 66–109. [[CrossRef](#)]
17. Terra, A.; Sergienko, G.; Gago, M.; Kreter, A.; Martynova, Y.; Rasinski, M.; Wirtz, M.; Loewenhoff, T.; Mao, Y.; Schwalenberg, D.; et al. Micro-Structuring of Tungsten for Mitigation of ELM-like Fatigue. *Phys. Scr.* **2020**, *2020*, 014045.
18. Terra, A.; Sergienko, G.; Tokar, M.; Borodin, D.; Dittmar, T.; Huber, A.; Kreter, A.; Martynova, Y.; Möller, S.; Rasiński, M.; et al. Micro-Structured Tungsten: An Advanced Plasma-Facing Material. *Nucl. Mater. Energy* **2019**, *19*, 7–12. [[CrossRef](#)]
19. Wang, B.; Hu, D.-Z.; Ma, D.; Lu, G.-H. Method for Improving Resistance of Fusion Reactor Inner Wall to Plasma Irradiation by Using Lamination Structure. U.S. Patent 10,102,928, 16 October 2018.
20. Wang, B.; Hu, D.-Z.; Ma, D.; Lu, G.-H. Improvement of irradiation resistance of the inner wall of a fusion stack using a laminated structure 2016. CN 201410117811.X, 17 February 2016.
21. Li, S.D.; Wang, B.; Liu, Y.H.; Qi, Y.F.; Li, M.; Ma, Y.T. Thermal Fatigue Resistance Enhancement of Laminated Copper Foil. *Chin. J. Vac. Sci. Technol.* **2018**, *38*, 434–441.
22. Xiao, S.; Ma, Y.; Tian, L.; Li, M.; Qi, C.; Wang, B. Decrease of Blistering on Helium Irradiated Tungsten Surface via Transversal Release of Helium from the Grooved Surfaces. *Nucl. Mater. Energy* **2020**, *23*, 100746. [[CrossRef](#)]
23. Li, C.; Zhu, D.; Li, X.; Wang, B.; Chen, J. Thermal-Stress Analysis on the Crack Formation of Tungsten during Fusion Relevant Transient Heat Loads. *Nucl. Mater. Energy* **2017**, *13*, 68–73. [[CrossRef](#)]
24. Davis, J.W.; Smith, P.D. ITER Material Properties Handbook. *J. Nucl. Mater.* **1996**, 233–237, 1593–1596. [[CrossRef](#)]
25. Wang, S.-M.; Li, J.-S.; Wang, Y.-X.; Zhang, X.-F.; Ye, Q. Thermal Shock Behavior Analysis of Tungsten-Armored Plasma-Facing Components for Future Fusion Reactor. *Acta Met. Sin. Engl. Lett.* **2018**, *31*, 515–522. [[CrossRef](#)]
26. Wang, L.; Wang, B.; Li, S.-D.; Ma, D.; Tang, Y.-H.; Yan, H. Thermal Fatigue Mechanism of Recrystallized Tungsten under Cyclic Heat Loads via Electron Beam Facility. *Int. J. Refract. Met. Hard Mater.* **2016**, *61*, 61–66. [[CrossRef](#)]
27. Zhao, M.; Zhou, Z.; Zhong, M.; Tan, J.; Lian, Y.; Liu, X. Thermal Shock Behavior of Fine Grained W-Y<sub>2</sub>O<sub>3</sub> Materials Fabricated via Two Different Manufacturing Technologies. *J. Nucl. Mater.* **2016**, *470*, 236–243. [[CrossRef](#)]
28. Xie, Z.M.; Miao, S.; Liu, R.; Zeng, L.F.; Zhang, T.; Fang, Q.F.; Liu, C.S.; Wang, X.P.; Lian, Y.Y.; Liu, X.; et al. Recrystallization and Thermal Shock Fatigue Resistance of Nanoscale ZrC Dispersion Strengthened W Alloys as Plasma-Facing Components in Fusion Devices. *J. Nucl. Mater.* **2017**, *496*, 41–53. [[CrossRef](#)]

29. Nemati, N.; Manhard, A.; Greuner, H.; Hunger, K.; Böswirth, B.; Visca, E.; You, J.H. Microstructural Evolution of Tungsten under Thermal Loads: A Comparative Study between Cyclic High Heat Flux Loading and Isochronous Furnace Heating. *Nucl. Mater. Energy* **2023**, *36*, 101465. [[CrossRef](#)]
30. Prakash, C.; Lee, H.; Alucozai, M.; Tomar, V. An Analysis of the Influence of Grain Boundary Strength on Microstructure Dependent Fracture in Polycrystalline Tungsten. *Int. J. Fract.* **2016**, *199*, 1–20. [[CrossRef](#)]
31. Yin, C.; Terentyev, D.; Zhang, T.; Nogami, S.; Antusch, S.; Chang, C.-C.; Petrov, R.H.; Pardoen, T. Ductile to Brittle Transition Temperature of Advanced Tungsten Alloys for Nuclear Fusion Applications Deduced by Miniaturized Three-Point Bending Tests. *Int. J. Refract. Met. Hard Mater.* **2021**, *95*, 105464. [[CrossRef](#)]
32. Jin, Y.-Z.; Liu, X.; Lian, Y.-Y.; Song, J.-P. Influence of Recrystallization on Tungsten Divertor Monoblock under High Heat Flux. *Tungsten* **2022**, *4*, 194–202. [[CrossRef](#)]
33. Lemetais, M.; Lenci, M.; Maurice, C.; Devictor, T.; Durif, A.; Minissale, M.; Mondon, M.; Pintsuk, G.; Piot, D.; Gallais, L.; et al. Temperature Gradient Based Annealing Methodology for Tungsten Recrystallization Kinetics Assessment. *Fusion Eng. Des.* **2023**, *193*, 113785. [[CrossRef](#)]
34. Larsen, T.; Chmelar, K.; Larsen, B.L.; Nagy, P.; Wang, K.; Pantleon, W. Thermal Stability of Differently Rolled Pure Tungsten Plates in the Temperature Range from 1125 °C to 1250 °C. *Fusion Eng. Des.* **2023**, *192*, 113581. [[CrossRef](#)]
35. Kim, H.C.; Bang, E.; Min, G.; Choi, H.; Han, H.N. Analysis of High Heat Flux Tested Tungsten Mono-Blocks by Hardness and Microstructural Profiling. *Fusion Eng. Des.* **2023**, *193*, 113800. [[CrossRef](#)]
36. Wu, X.-C.; Xu, L.-P. Quantitative Analysis and Evaluation of The Uddeholm Heat-Checking Scale. *Phys. Test. Chem. Anal. A Phys. Test.* **2002**, *38*, 14–17.
37. Qi, Y.; Tang, Y.; Wang, B.; Zhang, M.; Ren, X.; Li, Y.; Ma, Y. Characteristics of Tungsten Coatings Deposited by Molten Salt Electro-Deposition and Thermal Fatigue Properties of Electrodeposited Tungsten Coatings. *Int. J. Refract. Met. Hard Mater.* **2019**, *81*, 183–188. [[CrossRef](#)]

**Disclaimer/Publisher’s Note:** The statements, opinions and data contained in all publications are solely those of the individual author(s) and contributor(s) and not of MDPI and/or the editor(s). MDPI and/or the editor(s) disclaim responsibility for any injury to people or property resulting from any ideas, methods, instructions or products referred to in the content.